In-Situ Metrology of Large Segmented Detector Based on Modified Optical Truss

Qichang An, Hanfu Zhang, Xiaoxia Wu, Jianli Wang, Tao Chen, Jingxu Zhang, and Hongwen Li

***Abstract*—To precisely map cosmic structures and capture time-domain events, future large survey telescopes will be equipped with segmented detectors that greatly expand their field of view. Segment flatness and assembly accuracy will be essential for them to make accurate observations. Instead of physically measuring distances between adjacent mirror surfaces, our modified optical truss enables the angle (slope) between them to be calculated. Furthermore, we calculated the relative tilt and piston between the segmented detectors. The modified optical truss can measure the flatness of a mosaicked detector before and after it is assembled into a telescope. We reduced the volume, weight, and power of our device compared with earlier versions. Its angular accuracy is now better than 0.1 arcsecs, and, at a maximum scope of 500 μm, the linear accuracy of the new truss is better than 25 μm. In fact, accuracy and testing ranges are comparable to instruments found in optics labs.**

***Index Terms*—Large survey telescope, active optics, optical truss.**

I. Introduction

MAJOR scientific discoveries have been made through multi-messenger observation of the universe, such as the accelerating expansion of the universe and the existence of gravitational waves and exoplanets, leading to Nobel Prizes in 2011, 2017, and 2019 [1], [2], [3], [4].

Time-domain astronomy, an important area of future astronomy, requires large survey telescopes having stronger light-collecting ability, higher imaging resolution, and a broader collection spectrum within a wide field of view.

Focal plane detectors of large survey telescopes are comprised of multiple high-performance detectors mosaicked together. Their performance is limited by detector scale and budget. Ground-based telescopes, such as the 2.5 m survey telescope of the University of Science and Technology of China, the VLT Survey Telescope (VST), the Visible and Infrared Survey Telescope for Astronomy (VISTA) for the Southern Hemisphere, the Space Surveillance Telescope (SST) of the USA, and the Gaia Sky Survey Telescope of the ESA, are all equipped with large-format mosaicked detector arrays, as is the China Space Station Telescope (CSST) [5], [6], [7], [8].

Generally, if the field of an optical system is large, its depth of field (ability to focus) is correspondingly small. When a detector array at the focal plane significantly deviates from the flat, it causes defocusing, thereby reducing energy concentration and thus the highest stellar magnitude the telescope can detect [9].

In situ metrology of a large segmented detector is necessary to confirm the flatness of its detector array after it has been assembled into a telescope.

Flatness can be determined using:

- a three-coordinate measurement instrument (range: 100 mm; accuracy: 10 μm).
- white light interference methods (range: 100 mm; accuracy: 0.01 μm).
- geometric triangulation, limited by the reflectivity of the detector surface and interference of microstructures (range: 10 mm; accuracy: 1 μm).
- confocal scanning, limited to the axial dispersion area (range: 1 mm; accuracy: 0.1 μm) [10], [11], [12], [13], [14].

No measurement method can simultaneously achieve excellent range and accuracy. Moreover, because all such methods require a Precision Linear Displacement Stage,they cannot be used for real-time monitoring. Furthermore, in contrast to traditional flat detection of a continuous surface, the geometric error of a mosaicked detector is higher owing to its discontinuous steps.

In our experiment, we used the slope of wavefront to reconstruct the figure of merit of the detector. Instead of setting the pupil conversion optical path, we employed the simple, fast, and large dynamic range of In-situ Metrology of Large Segmented Detectors [15].

The flatness of a large mosaicked detector can be determined using slope measurements combined with frequency reconstruction, allowing the system to be adjusted accordingly. However, instead of measuring the distance between mirror surfaces, we investigated the use of a modified optical truss to obtain the angle (slope) of a multi-segment detector. Then, we determined the relative tilt and piston between the segmented detectors [16].

Manuscript received 8 February 2023; revised 16 March 2023; accepted 26 March 2023. Date of publication 29 March 2023; date of current version 6 April 2023. This work was supported in part by the Natural Science Foundation of China under Grants 12133009 and 62005279, in part by the Youth Innovation Promotion Association of the Chinese Academy of Science under Grant 2020221, and in part by Jilin Science and Technology Development Program under Grant 20220402032GH. *(Corresponding author: Qichang An.)*

Qichang An, Xiaoxia Wu, Jianli Wang, Tao Chen, Jingxu Zhang, and Hongwen Li are with the Changchun Institute of Optics, Fine Mechanics and Physics, Chinese Academy of Sciences, Changchun 130033, China, and also with the Jilin Provincial Key Laboratory of Intelligent Wavefront Sensing and Control, Changchun 130033, China (e-mail: anjj@mail.ustc.edu.cn; 4601389@qq.com; wangjianli@ciomp.ac.cn; chentaocdw@hotmail.com; zhangjx@ciomp.ac.cn; lihongwen@ciomp.ac.cn).

Hanfu Zhang is with the University of Chinese Academy of Sciences, Beijing 100039, China, and also with the Changchun Institute of Optics, Fine Mechanics and Physics, Chinese Academy of Sciences, Changchun 130033, China (e-mail: 1502597547@qq.com).

Digital Object Identifier 10.1109/JPHOT.2023.3262802

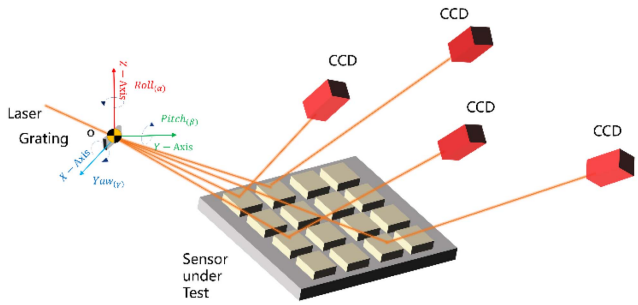

Fig. 1. Detection principle based on optical truss.

The remainder of this paper is organized as follows:

- Section II explains the principle and process of flatness measurement.
- Section III explains how simulation data were used to verify the accuracy of our measurement method.
- Section IV describes the experiments that we performed for testing and precision traceability.
- Section V summarizes the results of this study.

II. Experimental Principle

In this section, we explain the principle and process of our measurements, including our flatness detection procedure and data processing method.

We assumed that the detector surface was a Lambert radiator; that is, the detected brightness was independent of the observation angle. Therefore, we assumed a detector placed at any position where light can be received can produce an image with high robustness. Thus, the distribution law of light intensity remains Gaussian and is not affected by wavefront distortion. Therefore, when extracting the position of the image point, we used a Gaussian shape as the fitting template to determine the center position of the light point. Then, we estimated the slope based on the deviation of the position.

A laser metrology truss (Fig. 1) is a new measurement technique. It uses lasers to form a "truss" that combines geometric position changes and absolute phase measurements to achieve high-range measurements of the component pose.

This method, based on multiple -input and -output controls, can manage the dynamic pose and boundary changes of measured components and solve problems associated with single optical or electronic methods that are limited by communication bandwidth and integration time.

To calibrate the initial position of a light point, a plane mirror with an equal size aperture can be used in the laboratory, whereas a plane mirror with a small aperture can be used in situ.

Our method has a large measurement range, fast response, and large bandwidth (up to several kHz, if a high-speed detector is used).

We first calculated pose information based on our geometric configuration. Then, we physically constructed a uniformly split spatial beam using a grating. Finally, we detected the light-spot position using a photodetector that measured the reflection from the surface whose flatness was being assessed.

From the perspective of geometric optics, the ideal location of a detector matrix would be on a spherical surface. Otherwise, displacement of the light spot caused by two-dimensional deflection and axial movement of mosaicked detectors will cause the light spot to be off-center, reducing sensitivity.

Based on the calibration of a known precision flat, we obtained the initial position of the image point on the detector. Subsequently, we determined the focal plane using information obtained by varying the light spot on the target surface of the camera.

Light propagation can be modeled using point-slope-based spatial light equations and light-reflection matrices. For example, light starting from the origin point $O(x_0, y_0, z_0)^T$ (on the grating) and moving in the direction of $X_d = (x_d, y_d, z_d)^T$ can be expressed as:

$$\begin{cases} x &= x_d\, t + x_0 \\ y &= y_d\, t + y_0 \\ z &= z_d\, t + z_0 \end{cases} \tag{1}$$

Here, the direction vector has been normalized, and t is the distance the light beam travels from the origin point, $O(x_0, y_0, z_0)^T$. The equation of the plane on which the mirror is located is:

$$ax + by + cz + d \;=\; 0 \tag{2}$$

So, the intersection of the light and plane can be expressed as:

$$t_s = \; -\frac{ax_o + by_o + cz_o + d}{ax_d + by_d + cz_d}, \tag{3}$$

where t_s is the distance the light beam travels from the origin point $O(x_0, y_0, z_0)^T$.

We used the direction–transformation principle of light; namely, incident, normal, and outgoing light are located on the same plane, and incoming light and outgoing light are symmetrical with respect to the normal. The direction of ray propagation can be found through coordinate transformation.

The geometric position of a light spot on a target surface can be obtained through spatial tracing of each light wave beginning with the incident light of the system. Slope information is obtained from the difference in light intensity. Moreover, the exact position of the light spot on the target surface can be found by cross-comparison with the position of the incident point of the light, thereby reducing the effect of systematic errors.

Different stages of the adjustment process have different error modes. Because of the long optical path of the system, tilt error is most prevalent during preliminary adjustment. After initial inclination adjustment, the target surface, that is, the whole detector, may shift a short distance along the plane. The location of the image point may also move because of the tilt. However, tilt error can be reversed using geometry. When we adjust the tilt, the target surface moves a small distance in the normal direction of the mirror surface. That translation (or step) error shifts the position of the image point.

A mosaicked detector moves in the plane as a whole and encompasses the tilt of each sub-block detector. (See the red arrow in the lower half of Fig. 2.) When tilt is fully corrected,

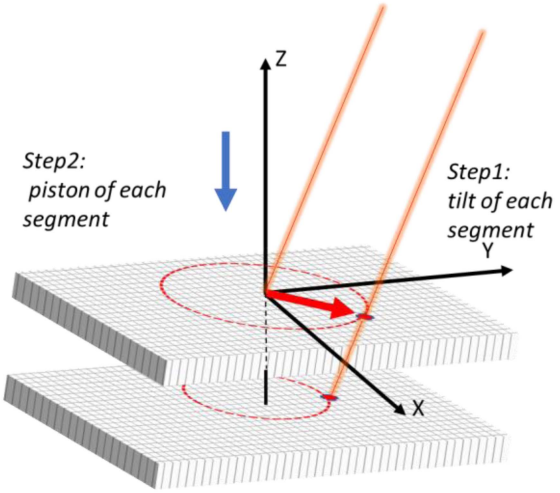

Fig. 2. Schematic of the light propagation model with only the step error in the detector.

any movement in the vertical direction must be wholly caused by piston error. If no change occurs in the light spot when the target surface is moved extremely slightly in the plane or normal direction, that means the focal plane has been fully adjusted. However, when we completed our adjustments, a small deviation from the ideal position still existed. (This residual deviation is called the mosaicked detector error.)

We obtained Fig. 2 using the slope-testing method, whereby the slope of each light ray is found using the difference in light intensity. For slope testing, we obtained detector surface shape through frequency domain integration. Considering the one-dimensional solution for light intensity as an example, (4) expresses the discrete Fourier transform:

$$X(k) = \sum_{n=0}^{N-1} x(n)\, e^{-j\frac{2\pi}{N}kn}, \tag{4}$$

where n and k are integers, N is the sequence length, and J is an imaginary unit. We assumed that $x(n)$ and $y(n)$ originate from the difference, as shown in (5):

$$x(n) = y(n+1) - y(n) \tag{5}$$

Substituting (4) into (5), we obtain (6):

$$\begin{aligned} X(k) &= \sum_{n=0}^{N-1} [y(n+1) - y(n)]\, e^{-j\frac{2\pi}{N}kn} \\ &= \sum_{n=0}^{N-1} y(n+1)\, e^{-j\frac{2\pi}{N}kn} - \sum_{n=0}^{N-1} y(n)\, e^{-j\frac{2\pi}{N}kn} \\ &= e^{j\frac{2\pi}{N}k} \sum_{n=0}^{N-1} y(n+1)\, e^{-j\frac{2\pi}{N}k(n+1)} + y(0) - y(0) \\ &\quad - \sum_{n=0}^{N-1} y(n)\, e^{-j\frac{2\pi}{N}kn} \end{aligned} \tag{6}$$

Substituting $Y(k) = \sum_{n=0}^{N-1} y(n) e^{-j\frac{2\pi}{N}kn}$ into (6) when k $>$ 1, we obtain:

$$X(k) = \left[e^{j\frac{2\pi}{N}k} - 1\right] Y(k) + e^{j\frac{2\pi}{N}k} y(n) - y(0) \tag{7}$$

And when $k = 0$,

$$X(0) = \sum_{n=0}^{N-1} [y(n+1) - y(n)] = y(N) - y(0) \tag{8}$$

An equivalent transformation can be obtained when k $\geq$ 1.

$$Y(k) = \frac{X(k)}{e^{j\frac{2\pi}{N}k} - 1} + \frac{e^{j\frac{2\pi}{N}k} y(n) - y(0)}{e^{j\frac{2\pi}{N}k} - 1} \tag{9}$$

Assuming the initial value of the original signal is y(0) = 0, and combining it with the inverse Fourier transform, we get

$$\begin{aligned} y(n) &= \frac{1}{N} \sum_{k=0}^{N-1} Y(k)\, e^{j\frac{2\pi}{N}nk} \\ &= \frac{1}{N} \sum_{k=1}^{N-1} \left[\frac{X(k)}{e^{j\frac{2\pi}{N}k} - 1} e^{j\frac{2\pi}{N}nk} + \frac{e^{j\frac{2\pi}{N}k} y(N)}{e^{j\frac{2\pi}{N}k} - 1} e^{j\frac{2\pi}{N}nk} \right] \\ &\quad + \frac{y(N)}{N} = \frac{1}{N} \sum_{k=1}^{N-1} \frac{X(k)}{e^{j\frac{2\pi}{N}k} - 1} e^{j\frac{2\pi}{N}nk} \\ &\quad + \frac{1}{N} \left[y(N) + \sum_{k=1}^{N-1} \frac{e^{j\frac{2\pi}{N}k} y(N)}{e^{j\frac{2\pi}{N}k} - 1} e^{j\frac{2\pi}{N}nk} \right], \end{aligned} \tag{10}$$

where n and k are integers, N is the sequence length, and J is an imaginary unit. By considering the real part on both sides to simplify the expression, we can obtain (11).

$$\begin{aligned} y(n) &= real\ [y(n)] = real \left[\frac{1}{N} \sum_{k=1}^{N-1} \frac{X(k)}{e^{j\frac{2\pi}{N}k} - 1} e^{j\frac{2\pi}{N}nk} \right] \\ &\quad + real \left[\frac{1}{N} \sum_{k=0}^{N-1} \frac{e^{j\frac{2\pi}{N}k} y(N)}{e^{j\frac{2\pi}{N}k} - 1} e^{j\frac{2\pi}{N}nk} \right] \end{aligned} \tag{11}$$

Here, $real[\frac{1}{N} \sum_{k=1}^{N-1} \frac{X(k)}{e^{j\frac{2\pi}{N}k}-1} e^{j\frac{2\pi}{N}nk}]$ is the integral algorithm expression, and

$$\Delta = real \left\{ \frac{1}{N} \left[y(N) + \sum_{k=1}^{N-1} \frac{e^{j\frac{2\pi}{N}k} y(N)}{e^{j\frac{2\pi}{N}k} - 1} e^{j\frac{2\pi}{N}nk} \right] \right\}$$

is the error of the algorithm.

In addition to using slope information for wavefront reconstruction, this method can be used to obtain the root mean square of the slope and to analyze and evaluate system alignment and wavefront information. The root mean square of the slope can directly characterize wavefront quality and have a direct relationship with the traditional root mean square through a transformation. It also has a good mapping relationship with traditional representation methods [17].

III. Test Simulation

In this section, we show how we verified our method using simulation and by performing targeted analyses at different

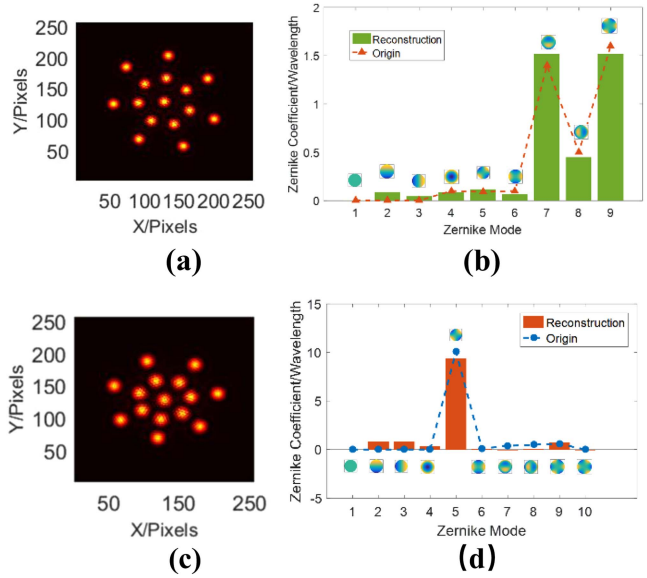

Fig. 3. Wavefront slope sampling and reconstruction accuracy. (a) Simulation of optical truss detection results under a small aberration. (b) Surface detection results under a small aberration. (c) Optical truss detection results under a large aberration. (d) Surface detection results under a large aberration.

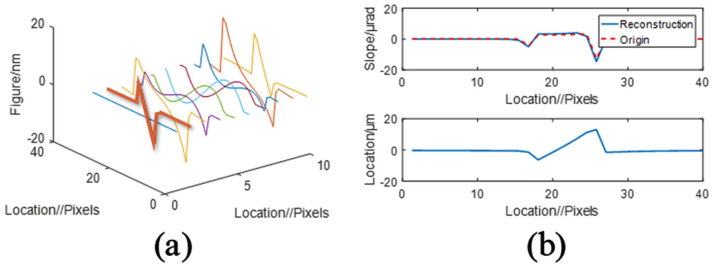

Fig. 4. Higher-order surface shapes and their sampling. (a) Slope of the reconstructed contour data compared with the original measured data. (b) Local reconstruction accuracy.

spatial frequencies. In large-aperture telescope system engineering, the detector target can be considered a low-order surface. Therefore, the comprehensive influence of piston/tip/tilt can be considered from the perspective of the overall surface shape of the multi-element detector. For the actual adjustment process, only local high points of low-order shape-fitting results need to be corrected. The low-order surface shape of the detector surface is fitted and can be characterized by its PV value (piston/tip/tilt comprehensive influence) because that value directly determines whether final imaging will be within the depth of focus.

A. Detector Figure Reconstruction

Here, reconstruction accuracy is analyzed based on the slope information obtained by combining the light point position movement and light path length. We reconstructed the flatness of the detector based on slope information. Fig. 3 shows our simulation results. According to the cross-sectional information, the main test errors are located at any edge, which means that they have little influence on the final topography measurement for adjusting the detector topography information of a large target surface.

Using the ability of the Zernike polynomial to characterize aberrations, we conducted a simulation. An accuracy better than 0.1 wavelength for a testing range of one wavelength was achieved. However, for a test range of 10 wavelengths, the accuracy was better than one wavelength. Thus, the accuracy of slope testing depends on the scope or range it covers.

It can be seen from Fig. 3 that this method can effectively extract the required low-order surface shape (the data can be used as a correction to the optical design model), whether it is a complex spatial frequency component or a single dominant spatial frequency. Specific adjustment of PV (piston/tip/tilt) can be obtained by local plane fitting for areas that do not meet depth-of-focus tolerance.

Fig. 4(a) shows the higher-order surface shapes and their samplings. Fig. 4(b) shows the slope of the reconstructed contour data compared with the original measured data for a typical surface shape. The accuracy was better than 0.1 wavelength. The figure shows that this method is well-suited for measuring both flat and steep surfaces.

B. Error Analysis

The structure-function (SF) represents the total energy of turbulent flow contained within a specific scale, which we later introduced into the evaluation of the system wavefront. It was intended to characterize surface undulations introduced by different processing or support methods at a specific scale. The basic definition of the structural function of the wavefront is given by:

$$SF\left(\lambda f\right) = \left\langle \left[W\left(u\right) - W\left(u + \lambda f\right)\right]^2 \right\rangle , \tag{12}$$

where **f** is the spatial coordinate, **u** is the characteristic frequency of the wavefront, W(u) is the complex amplitude after the pupil mask, λ is the wavelength, and $\langle \bullet \rangle$ is the average wavefront. Through an analysis of the structural function, we observed that the main characteristic spatial frequencies can all be reflected. For different spatial frequencies, we observed certain changes in the proportionality coefficients. Simultaneously, changes at the largest evaluation scale were mainly due to edge-down sampling (straight edges instead of round edges).

The CCD pixels were 10 μm on a side. Therefore, the detection area was 100 μm^2. Additionally, considering the geometric relationship between the Vignetting and spot size, the maximum detection range must have been greater than 10 mm.

At least two points are required in a single direction on each mosaicked detector sub-segment block. Fig. 5 shows how reconstruction surface structure functions correspond to different sampling rates. The actual introduced PV is 40 nm. The yellow-colored area represents the difference between the original surface structure function and the reconstructed wavefront. By comparison, it can be seen that at a lower sampling rate, a better characterization effect can be obtained. From the perspective of structure function, due to the sawtooth boundary, there will be additional offset near the aperture scale.

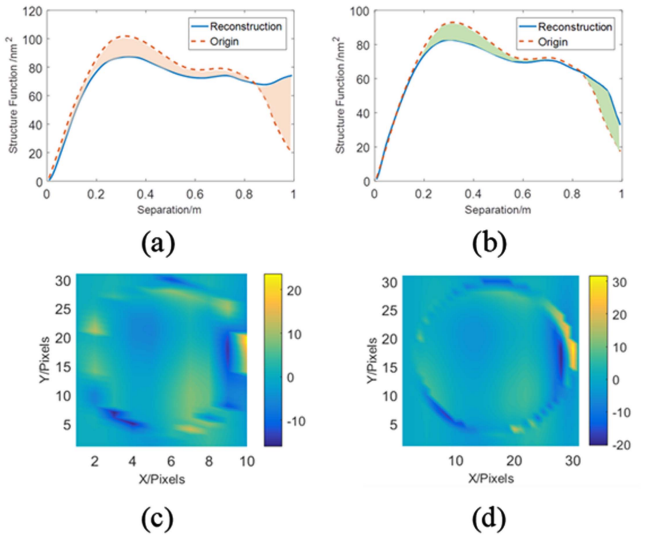

Fig. 5. Sampling rate structure function and error analysis. (a) High-sampling-rate structure function and error analysis. (b) Low-sampling-rate structure function and error analysis. (c) Reconstruction figure of the low sampling rate. (d) Reconstruction figure at a high sampling rate.

IV. Experimental Verification

We conducted experiments for testing and precision traceability using deformable mirrors to generate specific aberrations and existing algorithms to solve them.

Fig. 6(b) shows the simple optical system used for verification. A Gaussian beam uniformly distributed in space is formed using a laser and grating. The light-emitting position is above the axis of rotation symmetry of the system, and the angle between them is kept as small as possible ($< 5°$). The initial light spot position is fixed by flattening the deformable mirror. After voltage is applied, the surface shape of the deformable mirror changes, causing the light spot position to deviate from its original position. That offset, combined with the known distance information, enables surface reconstruction to be performed.

The grating has low heat sensitivity owing to its small size and low thermal inertia and can be used for in-situ detection under different temperature loads. We projected the point light source onto the deformable mirror after the light passed through the beam expander system. The light then entered the target surface of the detector through the lens group. When the system was perfectly aligned, with no aberration, the light spots on the detector were arranged evenly. In an actual system, because of aberration, the final light spot deviates to a certain extent. A deformation mirror can be used to detect the shape of the detector surface. The slope of the wavefront and corresponding system-pose information can be obtained by comparing the position of the light spot with its standard position. Yellow boxes show the light spot positions on the detector target.

In the actual detection process, due to inconsistency between the middle and edge parts of the detector substrate and processing error, the integrated effect of the system piston/tip/tilt was mostly manifested in a basic mode, such as coma/trefoil. Desktop experiments were conducted to verify these basic models.

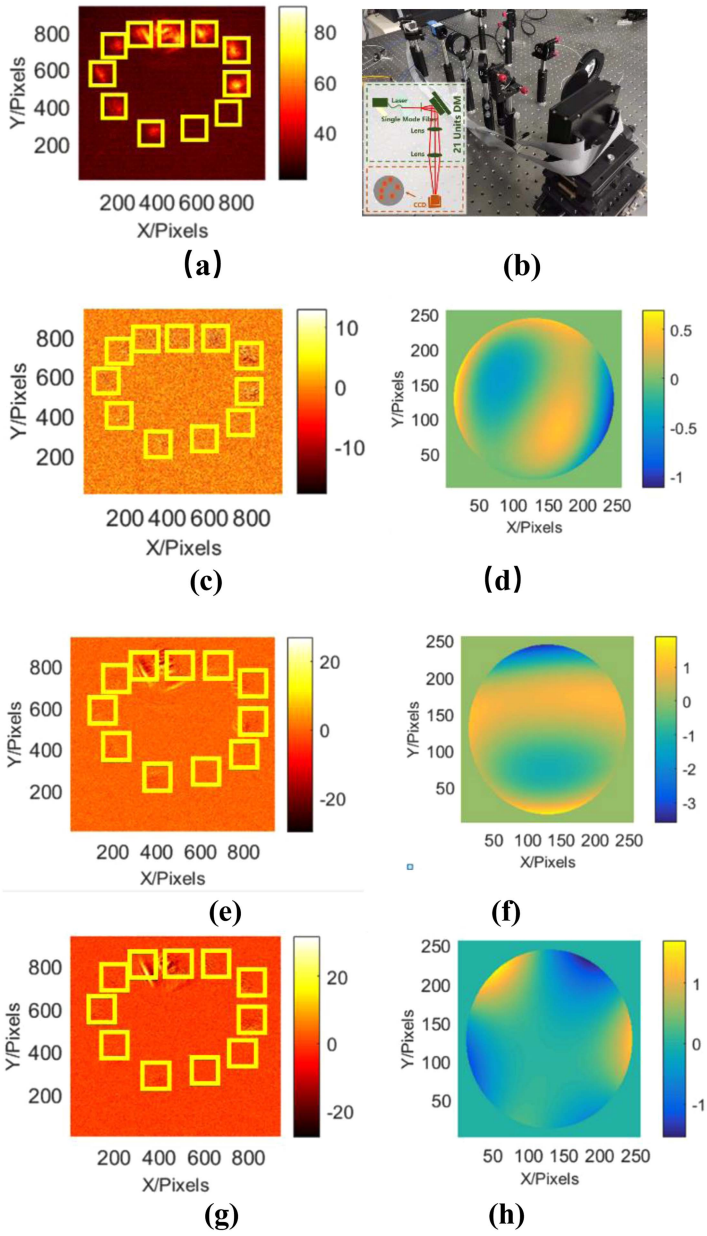

Fig. 6. Optical truss detection results. (a) Initial light point position detection site and experimental optical path. (b) Verification experimental system and its optical path diagram. (c) Light point intensity difference after adding a coma aberration. (d) Wavefront solution after adding a coma aberration. (e) Light point intensity difference after adding a coma aberration in the other direction. (f) Wavefront solution after adding a coma aberration in the other direction. (g) Light point intensity difference after adding a trefoil aberration. (h) Wavefront solution after adding a trefoil aberration.

Fig. 6 shows coma aberration in two different directions with the measured relative slope. As in [18], we used the Hartmann sensor to calibrate the accuracy of the aberration generation system. The precision traceability of detector flatness can be realized by using the flattening precision of the deformable mirror. The flattened shape precision of the deformable mirror was 1/20 of the wavelength (633 nm).

We amplified coma aberrations in different directions and generated trefoils with large amplitudes. The aberration type

is consistent with the added type. The root-mean-square error of the wavefront was within 0.1 wavelength for a wavelength of 633 nm.

According to precision-transfer principles, experimental measurement precision combines the squares of the flattening and measurement errors. This yields an accuracy of better than 0.1 wavelength in the 2-wavelength range. The focal length was 100 mm, and the angular accuracy was 0.1 arcsec. When the maximum scope was 500 μm, the accuracy was better than 25 μm at a wavelength of 633 nm.

V. Summary

Because of the small mass and high stability of our optical truss, it can be used for on-site, in-situ calibration purposes. Because the laser we used has good monochromaticity and strong directionality, it can be used for the detection of system spectral characteristics. Testing the flatness of large, mosaicked detectors on a slope has many advantages, such as high robustness and stability, non-interference, and anti-interference when compared with methods that use interference or wavefront sensing.

Acknowledgment

The authors would like to thank Dr. Hu and Dr. Wang for the help in testing. We would like to thank Editage (www.editage.cn) for English language editing.

Disclosures: The authors declare no conflicts of interest.

References

[1] M. H. Hill, "The theory of black hole formation shares the Nobel Prize in Physics," *Phys. Today*, vol. 73, no. 12, pp. 14–17, 2020.

[2] A. Grant, "Half of Nobel Prize in Physics honors exoplanet trailblazers," *Phys. Today*, vol. 72, no. 12, pp. 17–19, 2019.

[3] R. Genzel, *Massive Black Holes: Evidence, Demographics and Cosmic Evolution*. Cambridge, MA, USA: Birkhaüser, 2021, pp. 93–119.

[4] S. Lacour et al., "First direct detection of an exoplanet by optical interferometry–Astrometry and K-band spectroscopy of HR 8799 E," *Astron. Astrophys.*, vol. 623, 2019, Art. no. L11.

[5] A. M. Manuel, D. W. Phillion, S. S. Olivier, K. L. Baker, and B. Cannon, "Curvature wavefront sensing performance evaluation for active correction of the large synoptic survey telescope (LSST)," *Opt. Exp.*, vol. 18, no. 2, pp. 1528–1552, 2010.

[6] R. Holzlöhner, S. Taubenberger, A. P. Rakich, L. Noethe, P. Schipani, and K. Kuijken, "Focal-plane wavefront sensing for active optics in the VST based on an analytical optical aberration model," *Proc. SPIE*, vol. 9906, 2016, Art. no. 99066E.

[7] Z. Lou et al., "Advanced optical design and manufacturing technology and astronomical telescopes and instrumentation–Optical design study of the wide field survey telescope (WFST)," *Proc. SPIE*, vol. 10154, 2016, Art. no. 101542A.

[8] J. D. Bruijne, R. Kohley, and T. Prusti, "Gaia: 1,000 million stars with 100 CCD detectors," *Proc. SPIE*, vol. 7731, 2010, Art. no. 77311C.

[9] L. Guo et al., "Jitter-robust phase retrieval wavefront sensing algorithms," *Sensors*, vol. 22, no. 15, 2022, Art. no. 5584.

[10] R. Su and L.R. Leach, "Physics-based virtual coherence scanning interferometer for surface measurement," *Light, Adv. Manuf.*, vol. 2, no. 2, pp. 120–135, 2021.

[11] Q. An et al., "Large segmented sparse aperture collimation by curvature sensing," *Opt. Exp.*, vol. 28, no. 26, 2020, Art. no. 40176.

[12] Z. Geng, Z. Tong, and X. Jiang, "Review of geometric error measurement and compensation techniques of ultra-precision machine tools," *Light, Adv. Manuf.*, vol. 2, no. 14, pp. 2–14, 2019.

[13] P. Jia, R. Ning, R. Sun, and X. Yang, "Data-driven image restoration with option-driven learning for big and small astronomical image data sets," *Monthly Notices Roy. Astronomical Soc.*, vol. 501, no. 1, pp. 291–301, 2020.

[14] Q. An, H. Zhang, X. Wu, J. Wang, T. Chen, and G. Ju, "Curvature sensing-based pupil alignment method for large-aperture telescopes," *IEEE Photon. J.*, vol. 15, no. 1, Feb. 2023, Art. no. 6800705.

[15] A. Rakich, L. Dettmann, S. Leveque, and S. Guisard, "A 3D metrology system for the GMT," *Proc. SPIE*, vol. 9906, pp. 437–453, 2016.

[16] L. Zhao et al., "Cross-iteration multi-step optimization strategy for three-dimensional intensity position," *Opt. Exp.*, vol. 29, no. 18, pp. 29186–29201, 2021.

[17] Q. An, J. Zhang, F. Yang, and H. Zhao, "Normalized point source sensitivity analysis in GSSM prototype," *Chin. Opt. Lett.*, vol. 15, no. 11, 2017, Art. no. 111202.

[18] J. Hu, T. Chen, X. Lin, L. Wang, Q. An, and Z. Wang, "Improved wavefront reconstruction and correction strategy for adaptive optics system with a plenoptic sensor," *IEEE Photon. J.*, vol. 13, no. 4, Aug. 2021, Art. no. 6801008.